

MIT Open Access Articles

Universal linear optics by programmable multimode interference

The MIT Faculty has made this article openly available. **Please share** how this access benefits you. Your story matters.

Citation: Larocque, Hugo and Englund, Dirk. 2021. "Universal linear optics by programmable multimode interference." Optics Express, 29 (23).

As Published: 10.1364/OE.439341

Publisher: The Optical Society

Persistent URL: <https://hdl.handle.net/1721.1/144030>

Version: Final published version: final published article, as it appeared in a journal, conference proceedings, or other formally published context

Terms of Use: Article is made available in accordance with the publisher's policy and may be subject to US copyright law. Please refer to the publisher's site for terms of use.





Universal linear optics by programmable multimode interference

HUGO LAROCQUE^{1,2} AND DIRK ENGLUND^{1,3}

¹ Research Laboratory of Electronics & Department of Electrical Engineering and Computer Science, Massachusetts Institute of Technology, Cambridge, Massachusetts 02139, USA

² hlarocqu@mit.edu

³ englund@mit.edu

Abstract: We introduce a constructive algorithm for universal linear electromagnetic transformations between the N input and N output modes of a dielectric slab. The approach uses out-of-plane phase modulation programmed down to N^2 degrees of freedom. The total area of these modulators equals that of the entire slab: our scheme makes optimal use of the available area for optical modulation. We also present error correction schemes that enable high-fidelity unitary transformations at large N . This “programmable multimode interferometer” (ProMMI) thus translates the algorithmic simplicity of Mach-Zehnder meshes into a holographically programmed slab, yielding DoF-limited compactness and error tolerance while eliminating the dominant sidewall-related optical losses and directional-coupler-related patterning challenges.

© 2021 Optical Society of America under the terms of the [OSA Open Access Publishing Agreement](#)

1. Introduction

Rapid advances in photonic integrated circuits (PICs) have ushered in a new generation of devices capable of universal linear-optics transformations across a set of N optical modes [1]. These ‘programmable photonic circuits’ are enabling new applications ranging from quantum information processing [2,3] to deep learning [4]. In leading implementations, the mode transformations are realized as an $SU(N)$ rotation, which can be factored into $N(N-1)/2$ $SU(2)$ rotations [5]. Figure 1(a) illustrates the concept on input modes A_1, \dots, A_N , where $SU(2)$ rotations are programmed in Mach-Zehnder interferometers (MZIs), as shown in Fig. 1(b). A key advantage of this ‘MZI mesh’ (MZM) architecture is its compatibility with efficient programming algorithms [6,7]. But while tens of modes have been realized [1], the MZM architecture has inherent limitations – most importantly, the exacting fabrication requirements of 50:50 couplers, a large fraction of inter-waveguide ‘dead’ space, and architecture-constrained operating bandwidth and decomposition schemes [8,9].

Alternatively, could universal linear-optical transformations be deterministically programmed in a rectangular dielectric slab, a large ‘multimode interferometer’? We consider this question for the N transverse spatial modes of a slab with an index contrast quantified by $\sqrt{\Delta\epsilon/\epsilon_0}$, as shown in Fig. 1(c). This slab has single-mode thickness $L_y = \lambda/2\sqrt{\Delta\epsilon/\epsilon_0}$, length L_z , while the width L_x accommodates $N \sim 2L_x\sqrt{\Delta\epsilon/\epsilon_0}/\lambda$ transverse spatial modes. Recent experimental work did realize programmable 1×2 switching in a 2-mode MMI fabricated in silicon [10–12], but programming the index perturbations relied on a randomized search algorithm that lacks the algorithmic determinism of the MZM approach [6,7,13]. On the other hand, programming $SU(N)$ transformations by cascading layers of phase masks and Fourier planes [14–17] requires a total length of $O(N)$ elements [18], each of length $O(N)$. This device’s length therefore scales as $L_z \propto N^2$, whereas the minimum necessary scaling is $L_z \propto N$ to accommodate the necessary $N(N-1)$ phase shifters.

Here, we show that the compactness of MMIs and the programmability and $O(N)$ length scaling of MZMs are possible in one device: a programmable multimode interferometer (ProMMI) that relies on a mesh of $O(N^2)$ phase shifters distributed across a rectangular

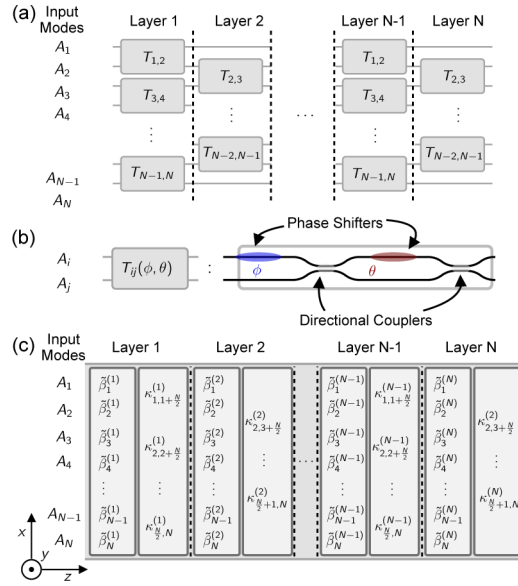


Fig. 1. SU(2) mesh architectures (a) Schematics of an SU(N) transformation decomposed into a rectangular mesh of SU(2) transformations T_{ij} . (b) Mach-Zehnder interferometer (MZI) used in integrated photonic platforms for implementing individual T_{ij} 's in the mesh. These building blocks consist of two phase shifters, where one of them is book-ended by directional couplers. (c) MMI approach to realizing SU(N) transformations. The latter are achieved by segmenting the waveguide into layers where programmed refractive index variations first alter the propagation constants $\beta_{m,n}$ of modes m, n to $\tilde{\beta}_{m,n}^{(l)}$ and subsequently couples them as parametrized by the coupling strength $\kappa_{mn}^{(l)}$.

waveguide slab. Waveguide sidewall scattering loss is largely eliminated in the large cross-section waveguide; transverse dimensions are reduced by ~ 1 order of magnitude compared to MZMs; fabrication challenges of 2×2 couplers are eliminated. The longitudinal dimension scales as $L_z = \max(\alpha_1 N, \alpha_2 N^2)$, where α_1, α_2 are coefficients that depend on the ProMMI material platform. We also translate recent hardware error correction methods from MZM [19] to ProMMI architectures, allowing substantial improvements in unitary transformation fidelity.

2. Results

Instead of operating on an array of meshed single mode waveguides, the ProMMI architecture implements SU(N) transformations on the eigenmodes of a slab. Here, the slab has a width $L_x = w$, allowing it to support N modes. As in the MZM scheme [7], we cascade these transformations into N layers performing SU(2) transformations on pairs of eigenmodes. But unlike the MZM, we apply these transformations via structured index perturbations that first modify a mode's propagation constant from β_m to $\tilde{\beta}_m$ and then couple modes m and n at a rate κ_{mn} . Each $(\tilde{\beta}_{m,n}, \kappa_{mn})$ has two DoFs as required to control, say, the independent variables of relative phase and amplitude. But, unlike MZMs, the ProMMI architecture overlays these perturbations. In this way, the ProMMI achieves the deterministic programmability and length scaling of the MZM, while collapsing its width to w , i.e., the minimum required for N transverse modes.

2.1. Coupled mode theory

We approximate the step-index slab as infinitely thick such that its permittivity $\epsilon_s(\mathbf{r}) = \epsilon_{\text{core}}$ for $|x| < w/2$ and $\epsilon_s(\mathbf{r}) = \epsilon_{\text{clad}}$ elsewhere. The bounded monochromatic transverse electric (TE) field

propagating along the waveguide in the z direction thus takes the form

$$\mathbf{E}(x, y, z) = u(x, y, z)e^{i\omega t}\hat{\mathbf{y}}, \quad (1)$$

where the $\hat{\mathbf{y}}$ component of the field, $u(\mathbf{r})$, can be expanded in the orthonormal TE eigenmode basis $\{A_n\}$ as

$$u(x, y, z) = \sum_n a_n(z)A_n(x, y)e^{-i\beta_n z}. \quad (2)$$

We use coupled mode theory [20] to find the permittivity perturbation of the form $\epsilon_{p,(m,n)}^{(l)}(\mathbf{r}) = \epsilon_{A,(m,n)}^{(l)}\epsilon_{L,(m,n)}^{(l)}(z)\epsilon_{T,(m,n)}^{(l)}(x, y)$ for the SU(2) rotation between modes m and n in the l^{th} layer of the ProMMI. Substituting $\mathbf{E}(x, y, z)$ into the wave equation

$$\nabla \times \nabla \times \mathbf{E} = \frac{\epsilon_s(\mathbf{r}) + \epsilon_{p,(m,n)}^{(l)}(\mathbf{r})}{c^2} \frac{\partial^2 \mathbf{E}}{\partial t^2}. \quad (3)$$

yields the coupled mode equations

$$\frac{\partial a_m}{\partial z} e^{-i\beta_m z} = \frac{1}{\beta_m} \sum_n a_n \epsilon_{A,(m,n)}^{(l)} \epsilon_{L,(m,n)}^{(l)}(z) \kappa_{mn}^{(l)} e^{-i\beta_n z}, \quad (4)$$

where $\kappa_{mn}^{(l)}$ is the coupling coefficient:

$$\kappa_{mn}^{(l)} = -\frac{i}{2} \frac{\omega^2}{c^2} \int A_m^*(x, y) \epsilon_{T,(m,n)}^{(l)}(x, y) A_n(x, y) dx dy. \quad (5)$$

To optimize the selective coupling between modes m and n , we therefore set $\epsilon_{L,(m,n)}^{(l)}(z) = \cos((\beta_m - \beta_n)z)$ and use Eq. (5) to determine $\epsilon_{T,(m,n)}^{(l)}(x, y)$ that maximizes $\kappa_{mn}^{(l)}$.

This $\epsilon_{p,(m,n)}^{(l)}(\mathbf{r})$ in principle allows coupling between other pairs of modes m', n' as indicated by the maximum transfer amplitude

$$\begin{aligned} \eta_{m'n'} &= \frac{2|\kappa_{m'n'}^{(l)}|}{\sqrt{4|\kappa_{m'n'}^{(l)}|^2 + (\beta_p - (\beta_{m'} - \beta_{n'}))^2}} \\ &= \frac{1}{\sqrt{1 + \left(\frac{\beta_p - (\beta_{m'} - \beta_{n'})}{2|\kappa_{m'n'}^{(l)}|}\right)^2}}, \end{aligned} \quad (6)$$

where $\beta_p = \beta_m - \beta_n$. Therefore, this cross-talk is suppressed when

$$|\kappa_{m'n'}^{(l)}|/|(\beta_m - \beta_n) - (\beta_{m'} - \beta_{n'})| \ll 1, \quad (7)$$

which can be achieved in practice by lowering $\epsilon_{A,(m,n)}^{(l)}$. This residual coupling can also occur with the unbounded modes of the system, which increases with the strength of the perturbation, as quantified by κ , and the proximity of the bounded and unbounded modes in k -space. Such coupling thereby adds an additional source of loss to the structure as discussed in the next section.

We set the propagation constants $\tilde{\beta}_m^{(l)}$ in layer l (Fig. 1(c)) with the transverse perturbations $\epsilon_{T,(m,n)}^{(l)}(x, y)$ while turning off the mode coupling term, i.e., $\epsilon_{L,(m,n)}^{(l)}(z) = 1$. Across the full layer l

of length L_{layer} , the perturbation $\epsilon_{p,(m,n)}^{(l)}(\mathbf{r})$ thus transforms modes m and n as

$$T_{mn}^{(l)} = \begin{pmatrix} e^{-i\phi} \cos \theta & -i \sin \theta \\ -ie^{-i\phi} \sin \theta & \cos \theta \end{pmatrix}, \quad (8)$$

where $\theta = \kappa_{mn}^{(l)} L_{\text{layer}}/2$ is set by the mode coupler and $\phi = ((\tilde{\beta}_m^{(l)} - \tilde{\beta}_n^{(l)}) - (\beta_m^{(l)} - \beta_n^{(l)})) L_{\text{layer}}/2$ by the phase shifting perturbations. This m, n SU(2) transformation is the basic building block of our SU(N) decomposition algorithm, which is similar to the Clements scheme [7], as detailed in Supplement 1.

By this procedure, we determine all the necessary permittivity perturbations $\epsilon_{p,(m,n)}^{(l)}$ to construct the total perturbation $\epsilon_p^{(l)}(\mathbf{r}) = \sum_{(m,n)} \epsilon_{p,(m,n)}^{(l)}(\mathbf{r})$ in layer l . We repeat the process for all l to complete the desired SU(N) on the slab's eigenmodes.

2.2. 4-mode transformation

Let's consider an exemplary unitary transformation SU(4) on the TE modes of a $N = 4$ slab waveguide, with matrix elements:

$$\frac{1}{\sqrt{2}} \begin{pmatrix} -i & 0 & 0 & 1 \\ 0 & -i & 1 & 0 \\ i & 0 & 0 & 1 \\ 0 & i & 1 & 0 \end{pmatrix}. \quad (9)$$

Fig. 2(a) shows the $T_{mn}^{(l)}$ building blocks of each layer: the refractive index shifts Δn corresponding to four phase-shift perturbations with $\epsilon_{L,(m,n)}^{(l)}(z) = 1$ and the coupling perturbations with $\epsilon_{L,(m,n)}^{(l)}(z) = \cos((\beta_m - \beta_n)z)$.

Figure 2(b) shows the index shift caused by the total perturbation $\sum_{(m,n),l} \epsilon_{p,(m,n)}^{(l)}(\mathbf{r})$ implementing Eq. (9). Figure 2(c) plots the $|E_y(x, 0, z)|^2$ of a trial input field $(a_1, a_3, a_2, a_0)^T = (0, 1, 0, 0)^T$. Here, we used a split-step Fourier method [21] to numerically propagate the optical fields. As expected, $|E_y|^2$ is flat during the first half of layer 1 given that the only eigenmode propagating in the waveguide experiences a global phase shift. No coupling occurs in the second half because $\epsilon_{p,(3,n)}^{(1)}(\mathbf{r}) = 0$. In the second layer, the field remains flat in the first half for the same reasons as it did in layer 1, whereas it is entirely converted to A_2 in the second half since $\kappa_{2,3}^{(2)} L_{\text{layer}}/2 = \pi/2$. The first half of $l = 3$ features a mostly flat field as in $l = 1, 2$ and partial conversion to A_0 as specified by $\kappa_{0,2}^{(3)} L_{\text{layer}}/2 = \pi/4$. The relative phase between A_0 and A_2 manifests in the beating pattern in the first half of $l = 4$ followed by the full conversion of A_2 to A_3 according to $\kappa_{2,3}^{(4)} L_{\text{layer}}/2 = \pi/2$ in the second half. Fig. 2(d) plots the transmission of the ProMMI, as quantified by the absolute square of the bounded field, i.e. $T = \sum_{i=0}^3 |a_i|^2$. The drops observed in the second halves of each layer indicate stronger scattering to the unbounded modes of the system, as expected from the more rapid spatial variations of permittivity in these regions. In Fig. 2(e), (f), we provide the expansion coefficients of the field and compare them to those obtained directly from Eq. (8).

For further insight, it helps to view the transformation problem in k -space. Figure 2(g) shows the Fourier transform of the field in Fig. 2(c) as it enters the phase-shifting and coupling sections of each layer. Markers located at the central \mathbf{k} value of each eigenstate represent their relative weights. The perturbations $\epsilon_{p,(m,n)}^{(l)}$ couple modes m, n at a rate $\kappa_{mn}^{(l)}$ — they are therefore the

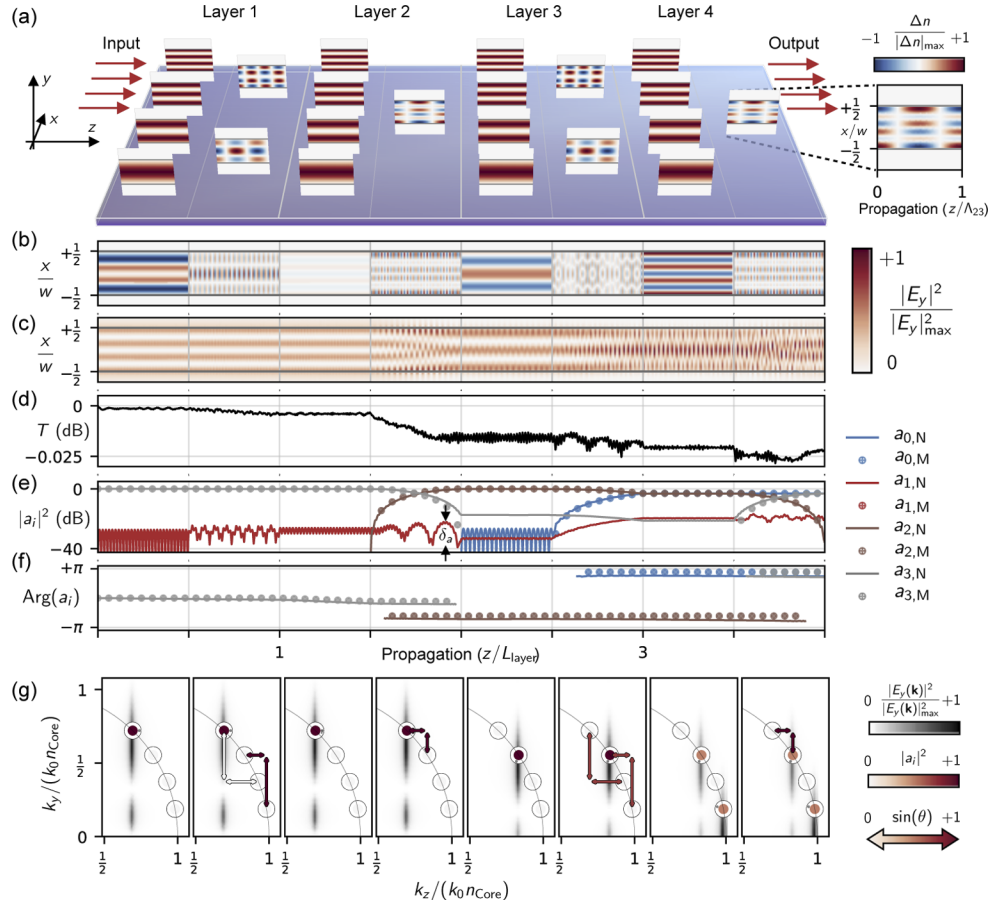


Fig. 2. ProMMI architecture of a 4-mode slab waveguide. (a) Structured refractive index perturbations used for arbitrary SU(4) transformations. The location of each perturbation matches that of the parameter it modifies according to Fig. 1(c). Inset: refractive index perturbation used to couple the waveguide's TE2 mode to the TE3 mode, where $\Lambda_{23} = 2\pi/(\beta_2 - \beta_3)$. (b) Refractive index perturbations required to induce the SU(4) transformation provided in Eq. (9). (c) Intensity of the optical field upon propagating through the perturbed waveguide for an input mode defined as $(a_1, a_3, a_2, a_0)^T = (0, 1, 0, 0)^T$, which in our architecture, consists of the waveguide's TE3 mode. Refractive indices of $n_{\text{core}} = 2.2886$ and $n_{\text{clad}} = 1.44$ were assigned to the core and the cladding of the waveguide, respectively, and we considered an optical wavelength of $1.55 \mu\text{m}$. (d) Weight of the field in (c) contained in the bounded modes of the device. (e) Absolute square and (f) phase values of the mode expansion coefficients, $a_{i,N}$, of the simulated field in (c) overlaid onto circular markers plotting the coefficients, $a_{i,M}$, expected from Eq. (8). (g) Optical transformations in each layer represented in k -space. The density plots show the absolute square of the field's Fourier transform at the start of the phase shifting and coupling sections of each layer. Markers located at each mode's central \mathbf{k} value are colored based on their weight and the angular position of the dot on their outline corresponds to their phase. Vertical and horizontal arrows indicate the propagation constant shifts enabled by the $\epsilon_{L,(m,n)}^{(l)}$ and $\epsilon_{T,(m,n)}^{(l)}$ components of the permittivity perturbations $\epsilon_{p,(m,n)}^{(l)}$, respectively, and are colored based on their corresponding θ values.

‘ k -space’ analog of the MZI SU(2) rotations. Thus, the ProMMI is the ‘ k -space’ realization of an MZM programmable unitary that, however, is inherently more compact and does not need single-mode patterning.

2.3. Error correction

To further gauge the reliability of our architecture, we performed the mode propagation simulations shown in Fig. 2 for 50 Haar random SU(4) rotations, U . We extracted the corresponding transmission matrix of the ProMMI from these simulations, U_{exp} , and thereafter the fidelity of the transformation, $F(U_{\text{exp}}, U) = |\text{Tr}(U^\dagger U_{\text{exp}}) / (N \text{Tr}(U_{\text{exp}}^\dagger U_{\text{exp}}))^{1/2}|^2$ [7]. Limits in the fidelity of these transformations arise from perturbations $\epsilon_{p,(m,n)}^{(l)}(\mathbf{r})$ being partially phased-matched to couple modes $m' \neq m$ and $n' \neq n$. These conditions increase the maximum transfer amplitude $\eta_{m'n'}$ defined in Eq. (6), causing transformations $T_{mn}^{(l)}$ to deviate from the block-diagonal form in Eq. (8). For instance, $\eta_{23} \sim 0.005$ in the second half of layer 2 from Fig. 2, explaining the oscillation in $|a_1|^2$ (see Fig. 2(e)) with an amplitude δ_a of roughly 0.5% of $|a_2|^2$ in that region of the ProMMI. The cross-talk introduced by this process consequently weakens the validity of our proposed SU(N) decomposition. However, as shown in Fig. 3(a), we can use additional optimization methods to further increase the fidelity of these transformations by altering the relative strengths of $\epsilon_{p,(m,n)}^{(l)}$. The cross-talk can also be mitigated by globally decreasing the strengths of $\epsilon_{p,(m,n)}^{(l)}$, albeit at the expense of increasing the total length of the device.

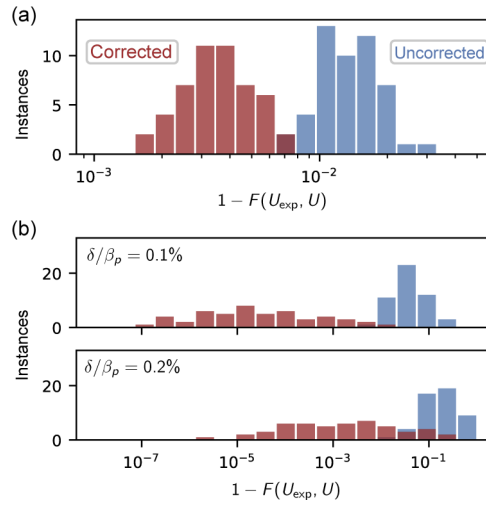


Fig. 3. ProMMI error correction. (a) Device infidelity $1 - F(U_{\text{exp}}, U)$ before and after correcting for cross-talk due to partial phase matching with gradient descent optimization. (b) Infidelity in the unitaries constructed from phase mismatched versions of Eq. (8) before and after correcting for imperfect phase matching. To emulate the effect of variations in the waveguide width from one layer to another, each SU(2) considered in the unitary’s reconstruction was affected by a mismatch δ drawn from a normal distribution with a standard deviation of $\delta = \alpha\beta_p$. For the waveguide parameters considered in Fig. 2, α values of 0.1% and 0.2% correspond to width discrepancies of 1.5 nm and 3 nm, respectively.

As in the case of MZMs, hardware errors can further reduce fidelity. For MZMs, the dominant source of errors is faulty couplers that do not have a 50:50 splitting ratio. For the ProMMI, such errors occur when a perturbation $\epsilon_{p,(m,n)}^{(l)}(\mathbf{r})$ has a period $\Lambda_p \neq 2\pi/|\beta_m - \beta_n|$ due to fabrication errors in the MMI waveguide that shift $\beta_{m,n}$ from their target values. In this event, the coupling

between modes m and n is not perfectly phase-matched, which increases the coupling rate between these modes and constrains the off-diagonal terms of $T_{mn}^{(l)}$ to absolute values below unity. For instance, under these mismatched conditions, the bottom left element of $T_{mn}^{(l)}$ becomes

$$(T_{mn}^{(l)})_{21} \rightarrow -i \frac{\kappa_{mn}^{(l)} e^{i(\delta L_{\text{layer}}/2 - \phi)}}{\sqrt{\delta^2 + (\kappa_{mn}^{(l)})^2}} \sin \left(\sqrt{\delta^2 + (\kappa_{mn}^{(l)})^2} \frac{L_{\text{layer}}}{2} \right), \quad (10)$$

where $\delta = (\beta_m - \beta_n - \beta_p)/2$ and $\beta_p = 2\pi/\Lambda_p$. This modification reduces the validity of the θ and ϕ parameters obtained in a unitary's SU(2) decomposition. Though schemes such as gradient descent methods [22] could correct these errors, a pre-characterization of the ProMMI's perturbations can provide a more deterministic form of correction. Based on a similar scheme used for MZM hardware [19], we deduce that hardware error correction in ProMMIs first involve modifying $\kappa_{mn}^{(l)}$ to $\kappa_{mn}^{(l)'} = ((\kappa_{mn}^{(l)})^2 + \Delta\kappa^2)^{1/2}$, where to first order

$$\Delta\kappa^2 = \delta^2 \left(\frac{\tan(\kappa_{mn}^{(l)} z)}{\kappa_{mn}^{(l)} z} - 1 \right). \quad (11)$$

As shown in Fig. 3(b), letting $\kappa_{mn}^{(l)} \rightarrow \kappa_{mn}^{(l)'}$ with an additional modification in the ϕ parameter of Eq. (8) corrects the faulty mode couplers in the unitaries considered in Fig. 3(a). As shown in Supplement 1, δ is related to errors in waveguide width, Δw , and perturbation period, $\Delta\Lambda$, through $\delta \approx (\beta_m - \beta_n)(\Delta w/w - \Delta\Lambda/2\Lambda)$. As a result, errors in the MMI waveguide are suppressed in devices with more modes.

2.4. Scaling

The ProMMI dimensions scale favorably compared to the MZM. First, in both approaches, the device width scales linearly with N , $w = \alpha_{\text{MZM,ProMMI}} N$, as seen in Fig. 4(a). However, $\alpha_{\text{MZM}} \gg \alpha_{\text{ProMMI}}$ to allow for spacing between the MZM waveguides. Second, as shown in Fig. 4(b), both approaches have a length $L = \alpha_1 N$, where $\alpha_1 = 2L_\pi$ for the ProMMI and L_π is the distance for one phase-degree of freedom. L/N is higher for the MZM as this architecture must also include 50:50 couplers. However, to keep the cross-talk specified in Eq. (6) below a maximum value, $\eta_{m',n'}^{\text{max}}$, the device length L_z must be lower-bounded. With increasing N , the propagation constants β_m become more and more closely spaced, reducing the denominator in Eq. (6). To counter this increase, $\kappa_{m',n'}^{(l)}$ must be commensurately reduced, thereby increasing the device length. As detailed in Supplement 1, by solving for $\kappa_{m',n'}^{(l)}$, the maximum cross-talk constraint $\eta_{m',n'}^{\text{max}}$ implies a device length $L_z \geq \alpha_2 N^2$, where

$$\alpha_2 \approx \frac{\lambda}{n_{\text{core}}(1 - (n_{\text{clad}}^2/n_{\text{core}}^2))} \sqrt{\frac{1 - (\eta_{m',n'}^{\text{max}})^2}{(\eta_{m',n'}^{\text{max}})^2}}$$

The total device length L_z is the greater of the $O(N)$ and $O(N^2)$ length requirements, yielding $L_z = \max(\alpha_1 N, \alpha_2 N^2)$. Figure 4(b) shows this linear to quadratic cross-over for various values of $\eta_{m',n'}^{\text{max}}$ and a nominal L_π value used in state-of-the-art integrated lithium niobate modulators [23]. The cross-over happens when $\alpha_1 N = \alpha_2 N^2$, i.e., at $N = \alpha_1/\alpha_2$.

Some individual layers may need to be extended slightly to keep the total dielectric perturbation in layer l , $\sum_{(m,n)} \epsilon_{p,(m,n)}^{(l)}(\mathbf{r})$, below a practical maximum — for example, the power supply voltage. In such instances, we can lower all perturbation amplitudes by the same factor x_l and extend that layer's length by $1/x_l$.

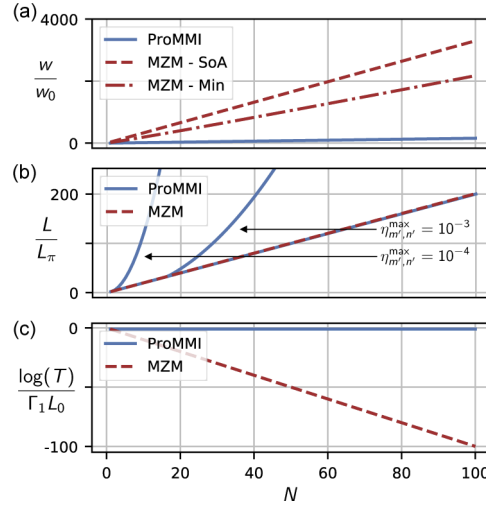


Fig. 4. Scaling properties of ProMMI vs MZM devices. (a) Device width in units of $w_0 = \lambda/\pi\sqrt{(n_{\text{core}}^2 - n_{\text{clad}}^2)}$. (b) Device length for both implementations in units of L_π . (c) Optical transmission expressed in units of $\Gamma_1 L_0$, where Γ_1 is the loss rate attributed to a single mode waveguide and L_0 is the layer length of the mode transformer. State-of-the art (SoA) values are attributed to SOI platforms equipped with thermo-optic phase shifters. The minimum width scaling in (a) is attributed to the waveguide spacing that leads to less than 1% cross-coupling between the waveguides of an MZM over its entire length.

Finally, the ProMMI architecture sharply curtails edge roughness losses due to reduced mode overlap. Since edge roughness commonly dominates the overall propagation loss rate Γ , we consider this advantage in detail. From coupled mode theory, the loss rate of the m^{th} eigenmode due to coupling to radiative modes is given by

$$\Gamma_m \propto |\kappa_{m\beta}|^2 \rho(\beta) \quad (12)$$

where $\rho(\beta)$ is the density of states attributed to radiative modes. The coupling coefficient $\kappa_{m\beta}$ is

$$\kappa_{m\beta} = -\frac{i}{2} \frac{\omega^2}{c^2} \int A_m^*(x, y) \epsilon_R(x, y) A_\beta(x, y) dx dy \quad (13)$$

where $\epsilon_R(x, y)$ is the permittivity perturbation causing radiative loss. For sidewall roughness, this perturbation is concentrated at the edges of the waveguide, i.e., $\epsilon_R(x) \approx \epsilon_R \delta(x - x_0)$, where the constant ϵ_R accounts for roughness and the Dirac delta function $\delta(x - x_0)$ centers on the sidewall. For such a perturbation, the coupling coefficient reduces to $\kappa_{m\beta} = -i(\omega^2/2c^2)\epsilon_R A_m^*(x_0) A_\beta(x_0)$, yielding a loss rate of

$$\Gamma_m \propto \left(\frac{\omega^2}{2c^2}\right)^2 \epsilon_R^2 A_m^2(x_0) |A_\beta(x_0)|^2 \rho(\beta) \quad (14)$$

where, on average, $A_m^2(x_0) \propto 1/N$. Thus, the loss rate in an N -mode waveguide is $\sim N$ times smaller than in a single-mode waveguide. As shown in Fig. 4(c), the ProMMI optical transmission relates to that of the MZM by $T_{\text{ProMMI}} \approx T_{\text{MZM}}^{1/N}$: i.e., losses are greatly reduced in the ProMMI when edge roughness dominates. Eliminating edge losses especially motivates ProMMI architectures in material platforms where smooth sidewalls are difficult to realize [23,24]. Other losses, possibly from active components, would then become dominant. To further reduce Γ_m , we can also lower ϵ_R by engineering waveguide edges [25], which are challenging to implement in MZMs.

3. Discussion

Material platforms for the ProMMI should be selected based on function. Applications demanding high-speed programmability would favor electro-optic (EO) waveguide materials, such as thin-film lithium niobate [23] or barium titanate [24]. These materials have exceptionally low material losses [26], which the ProMMI architecture can reach by suppressing otherwise dominant edge roughness losses. Moreover, residual $\propto 1/N$ edge roughness losses are actually further suppressed in otherwise problematic trapezoidal waveguide profiles [23,25]. Applications with relaxed modulation speed requirements could combine passive waveguide layers with existing large-scale phase modulators. For example, the modes in a slab of silicon nitride (SiN) covered in liquid crystals (LCs) could reach $\epsilon_{p,(m,n)}^{(l)}(\mathbf{r})/\epsilon_0 \sim 0.3$, combining excellent modulation contrast with the CMOS scalability of LC-on-silicon (LCOS) displays with millions of pixels.

The ProMMI operating spectrum is determined by the phase-matching requirement as seen from Eq. (6). Though a lower index modulation Δn reduces bandwidth, it reduces cross-talk due to partial phase-matching. This limitation is analogous to the bandwidth limitation due to modal dispersion in the couplers of MZMs. But whereas the MZM couplers are fixed, the ProMMI can be reprogrammed for different operating wavelengths – e.g., by using a regular electrode array of $>N^2$ pixels. A CMOS driver backplane is well suited to the task as commercial LCOS systems have millions of electrodes across an area of $\sim 1 \text{ cm}^2$. Alternatively, holographic techniques could efficiently program the $N(N-1)$ coupling perturbations into photorefractive crystals (such as lithium niobate) with $N(N-1)$ projected laser fields [27,28].

The ProMMI architecture is remarkable in another aspect: it saturates the compactness bound of programmable optical transformations in packing N^2 degrees of freedom as tightly as the material allows. Each ProMMI modal degree of freedom requires an area of $A_{\text{mode}} = NL\pi\lambda/\sqrt{n_{\text{core}}^2 - n_{\text{clad}}^2}$. Thus, assuming a lithium niobate ProMMI with an applied voltage of 0-1.5 V, a 1 cm^2 chip area would enable full programmability of $N \sim 90$ modes. The universality of the ProMMI programmability naturally extends to other waveguide geometries — for example, a MM waveguide bend, described by an N -dimensional unitary evolution U_{bend} , can be incorporated into the ProMMI transformation as $U = \prod_{(m,n),l=1}^N T_{m,n}^{(l)} \rightarrow (\prod_{(m,n),l=n+1}^N T_{m,n}^{(l)})U_{\text{bend}}(\prod_{(m,n),l=1}^n T_{m,n}^{(l)})$.

4. Conclusion

In conclusion, we introduced an architecture for programmable mode transformations that combines the best attributes of MZM and MMI constructions: (i) a constructive programming algorithm requiring the minimum N^2 control degrees of freedom; (ii) length scaling $\propto N$ for $N < \alpha_1/\alpha_2$ and otherwise $\propto N^2$; (iii) width scaling $\propto N$ but without the "dead-space" between MZM waveguides; (iv) edge roughness loss rates reduced by $O(1/N)$; (v) far easier waveguide fabrication as 50:50 couplers and bends are eliminated. Due to its large packing density, CMOS electronics are well suited to control the coupling perturbations. Holographic programming enables $N(N-1)$ control fields to control the $N(N-1)$ coupling perturbations. When combined with optical nonlinearities in the waveguide, the ProMMI architecture should be of great use in applications spanning deep learning [4,29] to physics-based simulators [30–32], to general-purpose quantum computing in photonic random walks [33]. Moreover, the ProMMI saturates 'control density': i.e., it is as compact as possible to fit $O(N(N-1))$ control degrees of freedom. This high control density, together with the potential for ultra-low optical loss and constructive programmability, will benefit applications ranging from LIDAR to virtual- and augmented-reality displays, to high-density telecom optical switches, machine learning accelerators, and optical quantum computing devices. We anticipate moreover that our approach extends beyond electromagnetic to other propagating bosonic fields, such as programmable multimode acoustic modes in a slab or magnons in 2D spin ensembles.

Funding. MITRE Quantum Moonshot Program; Natural Sciences and Engineering Research Council of Canada; National Science Foundation (ECCS-1933556); Defense Advanced Research Projects Agency (W911NF-20-1-0021).

Acknowledgments. The authors acknowledge Dr. Michael Fanto, Saumil Bandyopadhyay, Dr. Ryan Hamerly, and Prof. David A.B. Miller for fruitful discussions. Hugo Larocque acknowledges the support of the Natural Sciences and Engineering Research Council of Canada (NSERC), the MITRE Corporation Moonshot Program, the National Science Foundation (NSF, Award no. ECCS-1933556), and of the QISE-NET program of the NSF. D.E. acknowledges support from the Defense Advanced Research Projects Agency (DARPA, Grant no. W911NF-20-1-0021) ONISQ program.

Disclosures. The authors declare no conflicts of interest.

Data availability. Data underlying the results presented in this paper may be obtained from the authors upon reasonable request.

Supplemental document. See [Supplement 1](#) for supporting content.

References

1. W. Bogaerts, D. Pérez, J. Capmany, D. A. Miller, J. Poon, D. Englund, F. Morichetti, and A. Melloni, "Programmable photonic circuits," *Nature* **586**(7828), 207–216 (2020).
2. N. C. Harris, J. Carolan, D. Bunandar, M. Prabhu, M. Hochberg, T. Baehr-Jones, M. L. Fanto, A. M. Smith, C. C. Tison, P. M. Alsing, and D. Englund, "Linear programmable nanophotonic processors," *Optica* **5**(12), 1623–1631 (2018).
3. T. Rudolph, "Why i am optimistic about the silicon-photonics route to quantum computing," *APL Photonics* **2**(3), 030901 (2017).
4. G. Wetzstein, A. Ozcan, S. Gigan, S. Fan, D. Englund, M. Soljačić, C. Denz, D. A. Miller, and D. Psaltis, "Inference in artificial intelligence with deep optics and photonics," *Nature* **588**(7836), 39–47 (2020).
5. F. D. Murnaghan, *The orthogonal and symplectic groups* (Dublin Institute for Advanced Studies, 1958).
6. M. Reck, A. Zeilinger, H. J. Bernstein, and P. Bertani, "Experimental realization of any discrete unitary operator," *Phys. Rev. Lett.* **73**(1), 58–61 (1994).
7. W. R. Clements, P. C. Humphreys, B. J. Metcalf, W. S. Kolthammer, and I. A. Walmsley, "Optimal design for universal multiport interferometers," *Optica* **3**(12), 1460–1465 (2016).
8. D. S. Simon, C. A. Fitzpatrick, S. Osawa, and A. V. Sergienko, "Quantum simulation of discrete-time hamiltonians using directionally unbiased linear optical multiports," *Phys. Rev. A* **95**(4), 042109 (2017).
9. H. de Guise, O. Di Matteo, and L. L. Sánchez-Soto, "Simple factorization of unitary transformations," *Phys. Rev. A* **97**(2), 022328 (2018).
10. R. Bruck, K. Vynck, P. Lalan, B. Mills, D. J. Thomson, G. Z. Mashanovich, G. T. Reed, and O. L. Muskens, "All-optical spatial light modulator for reconfigurable silicon photonic circuits," *Optica* **3**(4), 396–402 (2016).
11. N. J. Dinsdale, P. R. Wiecha, M. Delaney, J. Reynolds, M. Ebert, I. Zeimpekis, D. J. Thomson, G. T. Reed, P. Lalan, K. Vynck, and O. L. Muskens, "Deep learning enabled design of complex transmission matrices for universal optical components," *ACS Photonics* **8**(1), 283–295 (2021).
12. M. Delaney, I. Zeimpekis, H. Du, X. Yan, M. Banakar, D. J. Thomson, D. W. Hewak, and O. L. Muskens, "Nonvolatile programmable silicon photonics using an ultralow-loss sb2se3 phase change material," *Sci. Adv.* **7**(25), eabg3500 (2021).
13. D. A. B. Miller, "Setting up meshes of interferometers – reversed local light interference method," *Opt. Express* **25**(23), 29233–29248 (2017).
14. J.-F. Morizur, L. Nicholls, P. Jian, S. Armstrong, N. Treps, B. Hage, M. Hsu, W. Bowen, J. Janousek, and H.-A. Bachor, "Programmable unitary spatial mode manipulation," *J. Opt. Soc. Am. A* **27**(11), 2524–2531 (2010).
15. G. Labroille, B. Denolle, P. Jian, P. Genevieux, N. Treps, and J.-F. Morizur, "Efficient and mode selective spatial mode multiplexer based on multi-plane light conversion," *Opt. Express* **22**(13), 15599–15607 (2014).
16. R. Tang, T. Tanemura, and Y. Nakano, "Integrated reconfigurable unitary optical mode converter using mmi couplers," *IEEE Photonics Technol. Lett.* **29**(12), 971–974 (2017).
17. M. van Niekirk, J. A. Steidle, G. A. Howland, M. L. Fanto, N. Soures, F. T. Zohora, D. Kudithipudi, and S. F. Preble, "Approximating large scale arbitrary unitaries with integrated multimode interferometers," in *Quantum Information Science, Sensing, and Computation XI*, vol. 10984 E. Donkor, M. Hayduk, M. R. Frey, S. J. L. Jr., and J. M. Myers, eds., International Society for Optics and Photonics (SPIE, 2019), pp. 146–152.
18. V. J. López-Pastor, J. S. Lundeen, and F. Marquardt, "Arbitrary optical wave evolution with fourier transforms and phase masks," arXiv:1912.04721 [quant-ph] (2019).
19. S. Bandyopadhyay, R. Hamerly, and D. Englund, "Hardware error correction for programmable photonics," *Optica* **8**, 1247–1255 (2021).
20. A. Yariv, "Coupled-mode theory for guided-wave optics," *IEEE J. Quantum Electron.* **9**(9), 919–933 (1973).
21. M. D. Feit and J. A. Fleck, "Light propagation in graded-index optical fibers," *Appl. Opt.* **17**(24), 3990–3998 (1978).
22. S. Pai, B. Bartlett, O. Solgaard, and D. A. B. Miller, "Matrix optimization on universal unitary photonic devices," *Phys. Rev. Appl.* **11**(6), 064044 (2019).

23. C. Wang, M. Zhang, X. Chen, M. Bertrand, A. Shams-Ansari, S. Chandrasekhar, P. Winzer, and M. Lončar, "Integrated lithium niobate electro-optic modulators operating at cmos-compatible voltages," *Nature* **562**(7725), 101–104 (2018).
24. S. Abel, F. Eltes, J. E. Ortmann, A. Messner, P. Castera, T. Wagner, D. Urbonas, A. Rosa, A. M. Gutierrez, D. Tulli, P. Ma, B. Baeuerle, A. Josten, W. Heni, D. Caimi, L. Czornomaz, A. A. Demkov, J. Leuthold, P. Sanchis, and J. Fompeyrine, "Large pockels effect in micro-and nanostructured barium titanate integrated on silicon," *Nat. Mater.* **18**(1), 42–47 (2019).
25. H. Lee, T. Chen, J. Li, K. Y. Yang, S. Jeon, O. Painter, and K. J. Vahala, "Chemically etched ultrahigh-q wedge-resonator on a silicon chip," *Nat. Photonics* **6**(6), 369–373 (2012).
26. M. Zhang, C. Wang, R. Cheng, A. Shams-Ansari, and M. Lončar, "Monolithic ultra-high-q lithium niobate microring resonator," *Optica* **4**(12), 1536–1537 (2017).
27. J. F. Heanue, M. C. Bashaw, and L. Hesselink, "Volume holographic storage and retrieval of digital data," *Science* **265**(5173), 749–752 (1994).
28. D. Psaltis and F. Mok, "Holographic memories," *Sci. Am.* **273**(5), 70–76 (1995).
29. Y. Shen, N. C. Harris, S. Skirlo, M. Prabhu, T. Baehr-Jones, M. Hochberg, X. Sun, S. Zhao, H. Larochelle, D. Englund, and M. Soljačić, "Deep learning with coherent nanophotonic circuits," *Nat. Photonics* **11**(7), 441–446 (2017).
30. D. N. Christodoulides, F. Lederer, and Y. Silberberg, "Discretizing light behaviour in linear and nonlinear waveguide lattices," *Nature* **424**(6950), 817–823 (2003).
31. F. Lederer, G. I. Stegeman, D. N. Christodoulides, G. Assanto, M. Segev, and Y. Silberberg, "Discrete solitons in optics," *Phys. Rep.* **463**(1-3), 1–126 (2008).
32. M. Segev, Y. Silberberg, and D. N. Christodoulides, "Anderson localization of light," *Nat. Photonics* **7**(3), 197–204 (2013).
33. Y. Lahini, G. R. Steinbrecher, A. D. Bookatz, and D. Englund, "Quantum logic using correlated one-dimensional quantum walks," *npj Quantum Inf.* **4**(1), 2 (2018).